remote sensing

MDPI

Article

Spatiotemporal Dynamics of Drought in the Huai River Basin (2012–2018): Analyzing Patterns Through Hydrological Simulation and Geospatial Methods

Yuanhong You [1,2,3], Yuhao Zhang [1,3], Yanyu Lu [2,*], Ying Hao [4], Zhiguang Tang [5] and Haiyan Hou [5]

[1] School of Geography and Tourism, Anhui Normal University, Wuhu 241002, China; youyuanhong@lzb.ac.cn (Y.Y.); yuhao@ahnu.edu.cn (Y.Z.)
[2] Anhui Province Key Laboratory of Atmospheric Science and Satellite Remote Sensing, Anhui Institute of Meteorological Sciences, Hefei 230031, China
[3] Engineering Technology Research Center of Resource Environment and GIS, Wuhu 241002, China
[4] Huaihe River Basin Meteorological Center, Anhui Meteorological Bureau, Hefei 230031, China; dg1328006@smail.nju.edu.cn
[5] National-Local Joint Engineering Laboratory of Geo-Spatial Information Technology, School of Earth Sciences and Geospatial Information Engineering, Hunan University of Science and Technology, Xiangtan 411201, China; tangzhg11@hnust.edu.cn (Z.T.); houhy@hnust.edu.cn (H.H.)
* Correspondence: ahqxlyy@163.com

Abstract: As climate change intensifies, extreme drought events have become more frequent, and investigating the mechanisms of watershed drought has become highly significant for basin water resource management. This study utilizes the WRF-Hydro model in conjunction with standardized drought indices, including the standardized precipitation index (SPI), standardized soil moisture index (SSMI), and Standardized Streamflow Index (SSFI), to comprehensively investigate the spatiotemporal characteristics of drought in the Huai River Basin, China, from 2012 to 2018. The simulation performance of the WRF-Hydro model was evaluated by comparing model outputs with reanalysis data at the regional scale and site observational data at the site scale, respectively. Our results demonstrate that the model showed a correlation coefficient of 0.74, a bias of −0.29, and a root mean square error of 2.66% when compared with reanalysis data in the 0–10 cm soil layer. Against the six observational sites, the model achieved a maximum correlation coefficient of 0.81, a minimum bias of −0.54, and a minimum root mean square error of 3.12%. The simulation results at both regional and site scales demonstrate that the model achieves high accuracy in simulating soil moisture in this basin. The analysis of SPI, SSMI, and SSFI from 2012 to 2018 shows that the summer months rarely experience drought, and droughts predominantly occurred in December, January, and February in the Huai River Basin. Moreover, we found that the drought characteristics in this basin have significant seasonal and interannual variability and spatial heterogeneity. On the one hand, the middle and southern parts of the basin experience more frequent and severe agricultural droughts compared to the northern regions. On the other hand, we identified a time–lag relationship among meteorological, agricultural, and hydrological droughts, uncovering interactions and propagation mechanisms across different drought types in this basin. Finally, we concluded that the WRF-Hydro model can provide highly accurate soil moisture simulation results and can be used to assess the spatiotemporal variations in regional drought events and the propagation mechanisms between different types of droughts.

Keywords: standardized index; WRF-Hydro model; soil moisture; drought characteristics

check for updates

Academic Editors: Liang Sun, Jianbin Su, Kun Zhang, Yushan Zhou and Zhiqing Peng

Received: 30 October 2024
Revised: 25 December 2024
Accepted: 9 January 2025
Published: 11 January 2025

Citation: You, Y.; Zhang, Y.; Lu, Y.; Hao, Y.; Tang, Z.; Hou, H. Spatiotemporal Dynamics of Drought in the Huai River Basin (2012–2018): Analyzing Patterns Through Hydrological Simulation and Geospatial Methods. *Remote Sens.* **2025**, *17*, 241. https://doi.org/10.3390/rs17020241

Copyright: © 2025 by the authors. Licensee MDPI, Basel, Switzerland. This article is an open access article distributed under the terms and conditions of the Creative Commons Attribution (CC BY) license (https://creativecommons.org/licenses/by/4.0/).

1. Introduction

Recent climate and environmental changes have led to a marked increase in the frequency and severity of disasters worldwide, with drought emerging as one of the most economically devastating events, affecting millions of people annually [1]. Each year, billions of dollars are allocated to mitigate the impacts of drought at both global and regional scales [2]. Moreover, the frequency and intensity of droughts are expected to intensify due to the ongoing effects of climate change [3]. Droughts are typically classified into four main categories: meteorological, agricultural, hydrological, and socio-economic [4]. Meteorological drought occurs when an imbalance between precipitation and evaporation results in a water deficit. Agricultural drought is defined by a significant decrease in soil moisture, which negatively impacts crop and pasture productivity [5,6]. Hydrological drought affects surface and subsurface water systems, leading to reduced streamflow or declining water levels in lakes and rivers [7,8].

Recent advances in drought monitoring highlight the dual challenges of achieving accurate long-term drought prediction and addressing the economic impacts on agriculture and water resources. Global Climate Models (GCMs), while valuable for large-scale climate forecasting, are limited by their coarse resolution, which reduces their effectiveness in predicting regional and extreme drought events [9]. To overcome these challenges, machine learning and deep learning techniques, such as logistic regression, gradient boosting, and random forest, have gained prominence for multi-factor drought prediction. These methods consistently outperform traditional statistical approaches in terms of their accuracy and adaptability [9]. Transformer models have also shown significant promise for geospatial prediction but face limitations when applied to long-term datasets due to their computational complexity and the need for extensive fine-tuning [9]. Emerging frameworks, such as XGBoost, effectively integrate hydrometeorological indices like the standardized precipitation index (SPI) with impact data, offering improved accuracy in quantifying drought effects on agriculture, biodiversity, and water resources [10]. Additionally, techniques such as the synthetic minority over-sampling technique and cost-sensitive learning address data imbalance, improving the models' ability to detect rare but impactful events like drought-induced wildfires [10]. Recent trends in drought prediction emphasize the integration of diverse and high-resolution data sources, including remote sensing, meteorological observations, and climate reanalysis data. Indicators like the Normalized Difference Vegetation Index (NDVI), land surface temperature, and soil moisture content, when combined with local climate indices, offer enhanced spatial and temporal representations of drought severity [11]. Hybrid modeling approaches, such as wavelet analysis coupled with support vector machines, further improve prediction accuracy by capturing non-linear and non-stationary patterns in drought dynamics [11]. These advancements underline the importance of combining innovative methodologies with interdisciplinary data sources to enhance our understanding and mitigation of drought impacts in a changing climate.

Drought types often evolve through drought propagation, involving complex interactions between meteorological, agricultural, and hydrological systems [12,13]. For instance, a precipitation deficit may propagate into hydrological systems, triggering agricultural drought in irrigated regions. This process is influenced by factors like the soil type, water storage capacity, and evapotranspiration rates [13,14]. Drought propagation, encompassing accumulation, attenuation, and extension, is crucial for understanding transitions between drought types and managing water resources effectively. In the Jinghe River Basin, China, a meteorological drought (SPI) was found to propagate into a hydrological drought (SRI) with a lag of approximately 127 days [15]. Furthermore, the study found that as drought propagates from meteorological to agricultural and hydrological phases, the frequency and duration of drought events decrease. Similarly, an investigation into the propagation of

meteorological drought to hydrological drought across three regions in China demonstrated a lag in the transition. The results showed that as meteorological droughts propagate into hydrological systems, their duration and severity intensify [16]. Studies across China further revealed that meteorological droughts generally precede hydrological droughts, with varying lag times influenced by the region and timescale. Different indices and timescales, such as SRI and SPEI, have been used to analyze drought propagation. For example, the one-month SRI correlates strongly with the two-month SPEI, particularly during dry seasons [17]. Timescale variations in indices like SSFI and SPI revealed differing sensitivities to drought events, highlighting the importance of selecting appropriate metrics to capture propagation dynamics effectively [18].

Land Surface Models (LSMs) are essential tools for predicting and analyzing drought characteristics, offering long-term simulations and incorporating variables like root zone soil moisture that are difficult to observe via satellite [19,20]. For example, the physically based, semi-distributed macro-scale Variable Infiltration Capacity (VIC) model has been employed to simulate the land surface water balance and hydrological drought in California's snowmelt areas, and the results demonstrated that the VIC model's monthly and seasonal hydrological drought simulations complemented meteorological drought predictions, effectively capturing the hydrological aspects of droughts [19]. Similarly, LSMs in Spain have demonstrated how precipitation influences hydrological variables like soil moisture and streamflow, affecting drought propagation dynamics [21]. Although the monthly SPI struggles to capture short-term drought, LSMs can provide finer temporal insights, overcoming observational limitations [22]. Recently, the Weather Research and Forecasting-Hydro (WRF-Hydro) model was developed to enhance the spatial resolution of land surface hydrological simulations, achieving resolutions as fine as 1 km or lower [23]. Evaluations in regions including the United States, Africa, and the Mediterranean show its strong performance in streamflow and runoff simulations [24–26]. Comparative studies with models like the Hydrologic Engineering Center-Hydrologic Modeling System (HEC-HMS) demonstrate that WRF-Hydro improves hydrological predictions by effectively simulating precipitation, enhancing the accuracy of drought and flood warnings [27].

The Huai River Basin (HRB), located in eastern China, functions as a transitional zone between the northern and southern climates of the country, making it particularly sensitive to climate change. In recent years, the spatiotemporal characteristics and mechanisms of drought events in the HRB have increasingly become a focal point of research, attracting growing attention from scholars. For instance, the SPI and SRI were used to represent meteorological and hydrological droughts in this basin. Moreover, the relationship between these indices was analyzed, and the results indicated that as the watershed area expands, the coherence between meteorological and hydrological droughts decreases, the lag effect of hydrological drought diminishes, and the correlation of drought propagation strengthens [27]. Another study, utilizing daily precipitation and runoff data from 16 sub-basins in the HRB, spanning the period from 1980 to 2014, quantitatively investigated the propagation relationship between meteorological and hydrological droughts [28]. This research also explored the impacts of climate, watershed characteristics, and human activities. The study found that climatic factors significantly influence the duration of hydrological drought, while watershed characteristics are strongly correlated with the severity, propagation time, and occurrence probability of type one drought propagation. Overall, the complexity and variability of drought propagation were underscored across different watershed scales in the HRB. Based on this consideration, in this study, the characteristics of droughts and their propagation from 2012 to 2018 were investigated using the WRF-Hydro model in the HRB.

The main goal of this study is to evaluate the performance of the WRF-Hydro model in simulating soil moisture in the HRB and to analyze the spatiotemporal characteristics of

meteorological, agricultural, and hydrological droughts during the study period. Section 2 introduces the study area, the WRF-Hydro model, the meteorological dataset, and the drought indices used in the analysis. Section 3 presents the simulation results of the WRF-Hydro model, compares the outcomes of various drought indices, and analyzes the spatiotemporal variation in drought events in the HRB. Finally, Section 4 summarizes the key findings of this study.

2. Material and Methods

2.1. Study Area

The HRB is located at the intersection of central and eastern China, spanning parts of Henan, Anhui, and Jiangsu provinces. Covering an area of approximately 270,000 square kilometers, its geographical coordinates range from 111°55′E to 121°25′E and 30°55′N to 36°36′N, as shown in Figure 1. The basin extends from the Tongbai and Funiu Mountains in the west to the Yellow Sea in the east. It is bordered by the Dabie Mountains, the Jianghuai Hills, several canals to the south, and the southern levee of the Yellow River and Mount Tai to the north, where it connects with the Yellow River Basin. The Huai River originates in the Tongbai Mountains and flows eastward through Henan, Anhui, and Jiangsu provinces before emptying into the Yellow Sea. Along its course, it is fed by numerous tributaries, influencing regions across Henan, Anhui, Jiangsu, and southern Shandong. As a transitional zone between northern and southern climates, the HRB plays a critical role in national grain production, energy, and manufacturing. However, it is particularly prone to droughts, which occur with high intensity and frequency. From 1991 to 2022, the HRB experienced some of the most severe and prolonged droughts among China's major river basins, with the peak drought event recorded in 2001. These persistent and severe droughts have profoundly impacted the regional hydrological cycle and agriculture, posing a significant threat to food security. The basin's diverse topography—characterized by mountainous and hilly areas in the west, southwest, and northeast areas, as well as expansive plains elsewhere—provides a natural laboratory for hydrological research and water resource management. Given the dual pressures of climate change and human activities, in-depth studies of the basin's hydrology are essential for safeguarding regional water and food security.

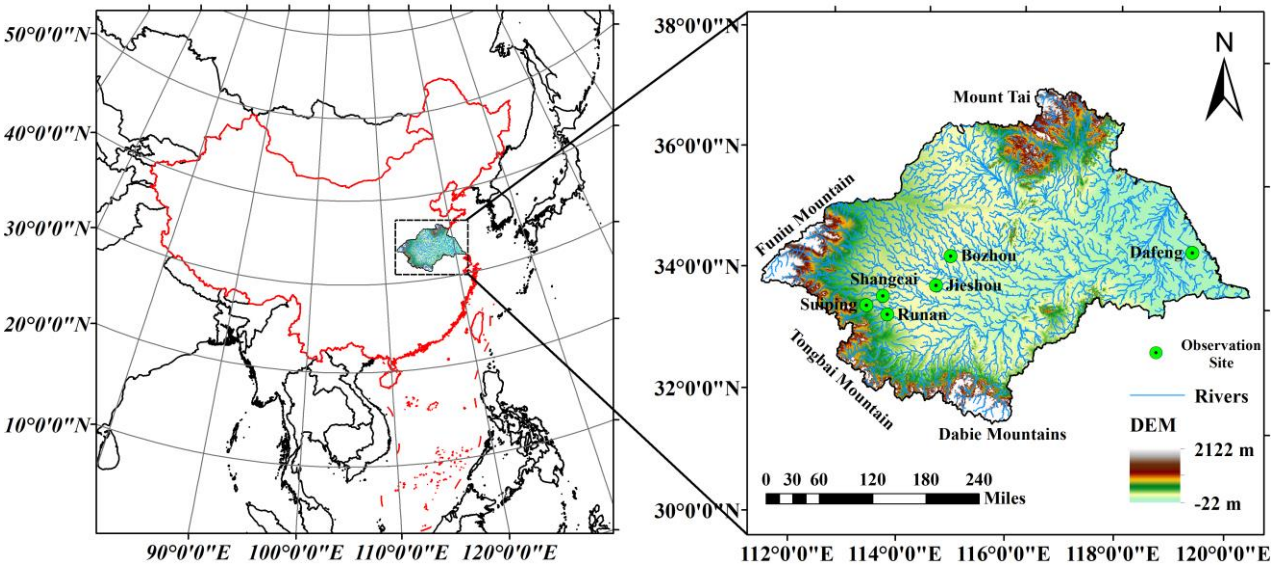

Figure 1. Elevation, river network, and observation stations for soil moisture data in the Huai River Basin.

To assess the accuracy of the model simulation results in this study, six observational sites within the study area were selected. These sites are listed as follows: Suiping site (elevation: ~53.4 m, 33.2731°N, 114.3011°E), Runan Station (elevation: ~50.1 m, 32.9608°N, 114.3461°E), Bozhou Station (elevation: ~39.1 m, 33.7833°N, 115.7333°E), Jieshou Station (elevation: ~38 m, 33.3333°N, 115.3667°E), and Dafeng Station (elevation: ~3.1 m, 33.1697°N, 120.4569°E). For evaluation purposes, daily soil moisture content data at a depth of 10 cm, recorded at around 9:00 AM throughout 2014, were obtained from these sites. Corresponding model-simulated values at the same locations were also utilized. A comparative analysis between the observed and simulated values was conducted to evaluate the model's simulation accuracy.

2.2. WRF-Hydro Model

The WRF-Hydro model is an advanced hydrological modeling tool developed from the Noah land surface process model within the Weather Research and Forecasting Model (WRF) framework. This model is specifically designed to simulate the interactions between atmospheric and hydrological processes. Supporting parallel processing, WRF-Hydro offers excellent scalability for large-scale simulations. This model can operate in a standalone (offline) mode or be coupled (online) with the WRF model to evaluate the impacts of climate change on hydrological systems. It leverages high-resolution surface data based on soil classification data from the US Geological Survey (USGS), Moderate-resolution Imaging Spectroradiometer (MODIS) land cover products, and the State Soil Geographic (STATSGO) data base. Additionally, it employs a diffusion wave model and a quasi-three-dimensional flow method to accurately capture the dynamics of surface runoff and subsurface lateral flow. In this study, the WRF-Hydro model was used in standalone mode, with simulations driven by hourly updated data. The spatial resolution was set to 0.05 degrees for the Land Surface Model grid and 0.005 degrees for the routing grid. The model was run for the period 2011–2018, with a one-year spin-up period in 2011 to ensure stabilization. Output data from 2012 to 2018 were utilized to analyze and quantify drought characteristics and propagation in the HRB.

2.3. Meteorological and Land Surface Data

To drive the standalone WRF-Hydro model, various meteorological data are required, including surface temperature, precipitation, humidity, wind direction, wind speed, longwave radiation, shortwave radiation, and air pressure. In this study, the China Meteorological Forcing Dataset (CMFD) from the National Tibetan Plateau Data Center was utilized. The CMFD is a high-resolution gridded near-surface meteorological dataset developed specifically for land surface process studies in China. It integrates remote sensing products, reanalysis datasets, and in situ observations from meteorological stations, providing data with an hourly temporal resolution and a spatial resolution of 0.05°. The CMFD includes seven near-surface meteorological elements: 2 m air temperature, surface pressure, specific humidity, 10 m wind speed, downward shortwave radiation, downward longwave radiation, and precipitation rate. The CMFD data outperformed satellite-derived products and other reanalysis data in terms of accuracy, particularly in the region of China's mainland [29]. The WRF-Hydro model requires surface information at the same resolution as the LSM grid (0.05° in this study), including digital elevation, land use, the leaf area index (LAI), albedo, and soil type. Additionally, high-resolution fields (0.005° routing grid in this study) are necessary for land and streamflow data, river order, and flow direction. These data were processed using HydroSheds (http://www.hydrosheds.org), derived from multi-scale Shuttle Radar Topography Mission (SRTM) data with a spatial resolution of 30 m. For the model performance evaluation, soil moisture data from the Global Land Data

Assimilation System (GLDAS) were used. The GLDAS data have a spatial resolution of 0.25° and a temporal resolution of 3 h intervals, representing soil moisture content at a depth of 0–10 cm within the HRB.

2.4. Evaluation Metrics

To evaluate the accuracy of the soil moisture simulation results from the WRF-Hydro model in the HRB, this study employed three commonly used statistical evaluation metrics: the Pearson correlation coefficient (CORR), bias (BIAS), and root mean square error (RMSE). These metrics provide complementary insights into the discrepancies between the model outputs and observed data, offering a comprehensive assessment of the model's precision and reliability.

The CORR is a statistical measure that quantifies the linear relationship between two variables, with values ranging from -1 to 1. A CORR value closer to 1 or -1 indicates a stronger positive or negative linear relationship, respectively, while a value near 0 suggests little to no linear relationship. The formula for calculating the CORR is given as follows:

$$r = \frac{\sum_{i=1}^{n}(y_i - \overline{y})(\hat{y}_i - \overline{\hat{y}})}{\sqrt{\sum_{i=1}^{n}(y_i - \overline{y})^2 \sum_{i=1}^{n}(\hat{y}_i - \overline{\hat{y}})^2}} \quad (1)$$

Here, $\overline{y}$ and $\overline{\hat{y}}$ represent the means of the observed and simulated values, respectively.

The BIAS metric measures the systematic deviation of the simulated values from the observed values. A positive BIAS indicates that the model tends to overestimate, while a negative BIAS suggests the underestimation of the observed values. The formula for calculating BIAS is given as follows:

$$Bias = \frac{1}{n}\sum_{i=1}^{n}(y_i - x_i) \quad (2)$$

Here, y_i represents the simulated values, and x_i denotes the corresponding observed values.

The RMSE quantifies the magnitude of differences between the simulated and observed values. It is defined as the square root of the average of the squared deviations between the simulated and observed data. The mathematical expression for RMSE is given as follows:

$$RMSE = \sqrt{\frac{1}{n}\sum_{i=1}^{n}(y_i - \hat{y}_i)^2} \quad (3)$$

Here, y_i represents the simulated values, $\hat{y}_i$ represents the observed values, and n is the number of observations. A smaller RMSE value indicates a smaller difference between the model's simulated results and the observed values, suggesting better model performance.

2.5. Drought Indices

In meteorological drought research, the SPI is a widely recognized metric, initially introduced by McKee et al. (1993) and based on long-term precipitation records. The SPI is computed by fitting precipitation data to a gamma distribution, which is subsequently transformed into a standard normal distribution, ensuring that the mean SPI value for any given location and time period is zero. The reliability of this approach is well-established, supported by the gamma distribution's strong alignment with precipitation data [30]. Building upon similar statistical foundations, this study also employs the SSMI and SSFI to evaluate agricultural and hydrological droughts, respectively [31]. To compute these

indices, this study utilized precipitation data from the CMFD, along with soil moisture and streamflow outputs from the WRF-Hydro model, focusing on the HRB. These indices are calculated from spatially averaged precipitation, soil moisture, and streamflow datasets. Monthly data spanning 2012 to 2018 were analyzed to investigate drought patterns and trends at a monthly scale within the basin. The calculations, following the methodologies of McKee et al., 1993 [31] and Angelidis et al. 2012 [32], involve the accumulation of precipitation, soil moisture, and streamflow data over specified time scales:

$$X_i^n = \sum_{t=0}^{n-1} (x_{i-t}) \tag{4}$$

In this study, x_i represents the variable value on the i th day, and X_i^k represents the accumulated variable value over a cumulative time scale of n months, with the time scale in this study being one month. The probability density function of the gamma distribution is described as follows:

$$g(x) = \frac{1}{\beta^{\alpha}\Gamma(\alpha)} x^{\alpha-1} e^{\frac{-x}{\beta}} \tag{5}$$

where α and β are the shape and scale parameters, respectively, x is the accumulated precipitation, and $\Gamma(\alpha)$ is the gamma function. The cumulative probability for a given time is calculated as follows:

$$G(x) = \int_0^x g(x)dx \tag{6}$$

For precipitation, there may be multiple zero values; therefore, when x = 0, the cumulative probability function of the gamma distribution is modified as follows:

$$H(x) = q + (1 - q)G(x) \tag{7}$$

where q is the probability of zero values, and $H(x)$ is the cumulative probability of the variable. Finally, the cumulative probability distribution is standardized to produce standardized indices (i.e., SPI, SSFI, and SSMI) as follows:

$$Standardizedindices = t - \frac{c_0 + c_1 t + c_2 t^2}{1 + d_1 t + d_2 t^2 + d_3 t^3}, t = \sqrt{ln\left(\frac{1}{(H(x))^2}\right)} \tag{8}$$

where c_0 = 2.55517, c_1 = 0.802853, c_2 = 0.010328, d_a = 1.432788, d_2 = 0.189269, and d_3 = 0.001308.

In this study, the standardized precipitation index (SPI), standardized soil moisture index (SSMI), and Standardized Streamflow Index (SSFI) were all calculated on a one-month time scale, denoted as SPI-1, SSMI-1, and SSFI-1, respectively. This notation emphasizes the uniform time scale adopted, ensuring consistency and facilitating the comparability of results across indices. The SSMI was derived using soil moisture data simulated by the WRF-Hydro model and supplemented by soil moisture observations from the GLDAS. This approach enabled the construction of a comprehensive time series of soil moisture for the HRB, providing a robust basis for assessing agricultural drought patterns and trends. Concurrently, the frequency and intensity of agricultural droughts were analyzed to assess the predictive capability of the WRF-Hydro model. Drought indices were employed to examine the various types of droughts and their propagation processes within the basin. The SPI was calculated using precipitation data from the CMFD to evaluate meteorological drought events in the region. A comparative analysis of the simulated SSMI and SPI was performed using line graphs to explore the relationship and correlation between meteorological and agricultural droughts, as well as their propagation mechanisms. Similarly,

the SSFI was derived from streamflow data simulated by the WRF-Hydro model and compared with the SPI obtained from CMFD data to elucidate the dynamic relationships and propagation mechanisms between meteorological and hydrological droughts. Drought events were defined based on a standardized index value below −1 [31,33]. Specifically, an SPI below −1 indicates the occurrence of a meteorological drought, an SSMI below −1 signals the onset of an agricultural drought, and an SSFI below −1 denotes the presence of a hydrological drought. Drought frequency was calculated as the percentage of months with a standardized index below −1 relative to the total number of months from 2012 to 2018. Drought intensity was determined by the minimum value of the standardized index during drought periods. By analyzing changes in the indices associated with meteorological, agricultural, and hydrological droughts, this study elucidates the propagation and correlation of these drought types. Furthermore, it provides a quantitative method for characterizing drought events through their frequency and intensity. Grid-based maps were generated to visualize the probability and severity of droughts at specific geographic locations within the HRB, offering valuable scientific insights for regional decision-makers in developing drought management and mitigation strategies. In this study, three major drought indices recommended by Guttman (1999) [34] were adopted: the SPI, SSMI, and SSFI. These indices measure dryness or wetness over specific time scales by comparing historical meteorological, soil, and hydrological data against long-term averages and standard deviations. Drought levels were classified based on index values, ranging from severe wetness to extreme drought, as detailed in Table 1:

Table 1. Classification of drought levels by standardized indices (SPI, SSMI, SSFI).

Drought Levels	SPI	SSMI	SSFI
No Drought	$0.5 < SPI \leq 2$	$0.5 < SSMI \leq 2$	$0.5 < SSFI \leq 2$
No Significant Drought	$-0.5 < SPI \leq 0.5$	$-0.5 < SSMI \leq 0.5$	$-0.5 < SSFI \leq 0.5$
Mild Drought	$-1.0 < SPI \leq -0.5$	$-1.0 < SSMI \leq -0.5$	$-1.0 < SSFI \leq -0.5$
Moderate Drought	$-1.5 < SPI \leq -1.0$	$-1.5 < SSMI \leq -1.0$	$-1.5 < SSFI \leq -1.0$
Severe Drought	$-2.0 < SPI \leq -1.5$	$-2.0 < SSMI \leq -1.5$	$-2.0 < SSFI \leq -1.5$
Extreme Drought	$SPI \leq -2.0$	$SSMI \leq -2.0$	$SSFI \leq -2.0$

3. Results and Discussion

3.1. Evaluation of WRF-Hydro Model Simulation Performance

In this section, we evaluate the simulation accuracy of the four soil moisture layers in the WRF-Hydro model using data from the GLDAS. The GLDAS provides soil moisture measurements at four depth intervals: 0–10 cm, 10–40 cm, 40–100 cm, and 100–200 cm, which align directly with the corresponding depth layers simulated by the WRF-Hydro model. Both the WRF-Hydro model output and the GLDAS dataset feature a temporal resolution of 3 h intervals. The GLDAS dataset combines observational data with climate model outputs, delivering high temporal and spatial resolutions over extended time periods. Its accuracy and reliability have been extensively validated in recent studies [35], making it a robust reference for model evaluation. Figure 2 presents scatter plots comparing the daily average soil moisture content simulated by the WRF-Hydro model at depths of 0–10 cm, 10–40 cm, 40–100 cm, and 100–200 cm with the corresponding GLDAS data for the period from 2012 to 2018. As shown in Figure 2, Subplot A represents the 0–10 cm depth, Subplot B represents the 10–40 cm depth, Subplot C represents the 40–100 cm depth, and Subplot D represents the 100–200 cm depth. Key findings include the following: for the 0–10 cm depth (Subplot A), the fitted regression equation is y = 0.83x + 4.18, with a CORR of 0.74, an RMSE of 2.66%, and a systematic BIAS of −0.29. The simulation results for this layer exhibit better agreement with the GLDAS data compared to the deeper soil layers. In the 10–40 cm depth layer (Subplot B), the slope of the fitted regression equation is 0.52,

while for the 40–100 cm depth (Subplot C), the slope is 0.41. These results highlight a progressive decline in agreement between the WRF-Hydro model and GLDAS data as soil depth increases. Overall, the WRF-Hydro model demonstrates the highest accuracy in simulating soil moisture in the 0–10 cm layer. This superior performance in the topsoil can be attributed to several factors. First, near-surface soil moisture is heavily influenced by atmospheric conditions such as precipitation and evaporation, which are well-captured in the WRF-Hydro model. Second, processes such as rainfall interception by vegetation and the direct effects of solar radiation are more accurately modeled in the upper soil layer. Although the WRF-Hydro model operates at a spatial resolution of 0.05 degrees and the GLDAS data operate at 0.25 degrees, both datasets share a 3 h temporal resolution. The strong correlation in the 0–10 cm layer suggests that differences in spatial resolution have minimal impact on the accuracy of simulation results at this depth. This analysis underscores the capability of the WRF-Hydro model to accurately simulate soil moisture at finer spatial resolutions, particularly in the topsoil layer, while maintaining high consistency with GLDAS data.

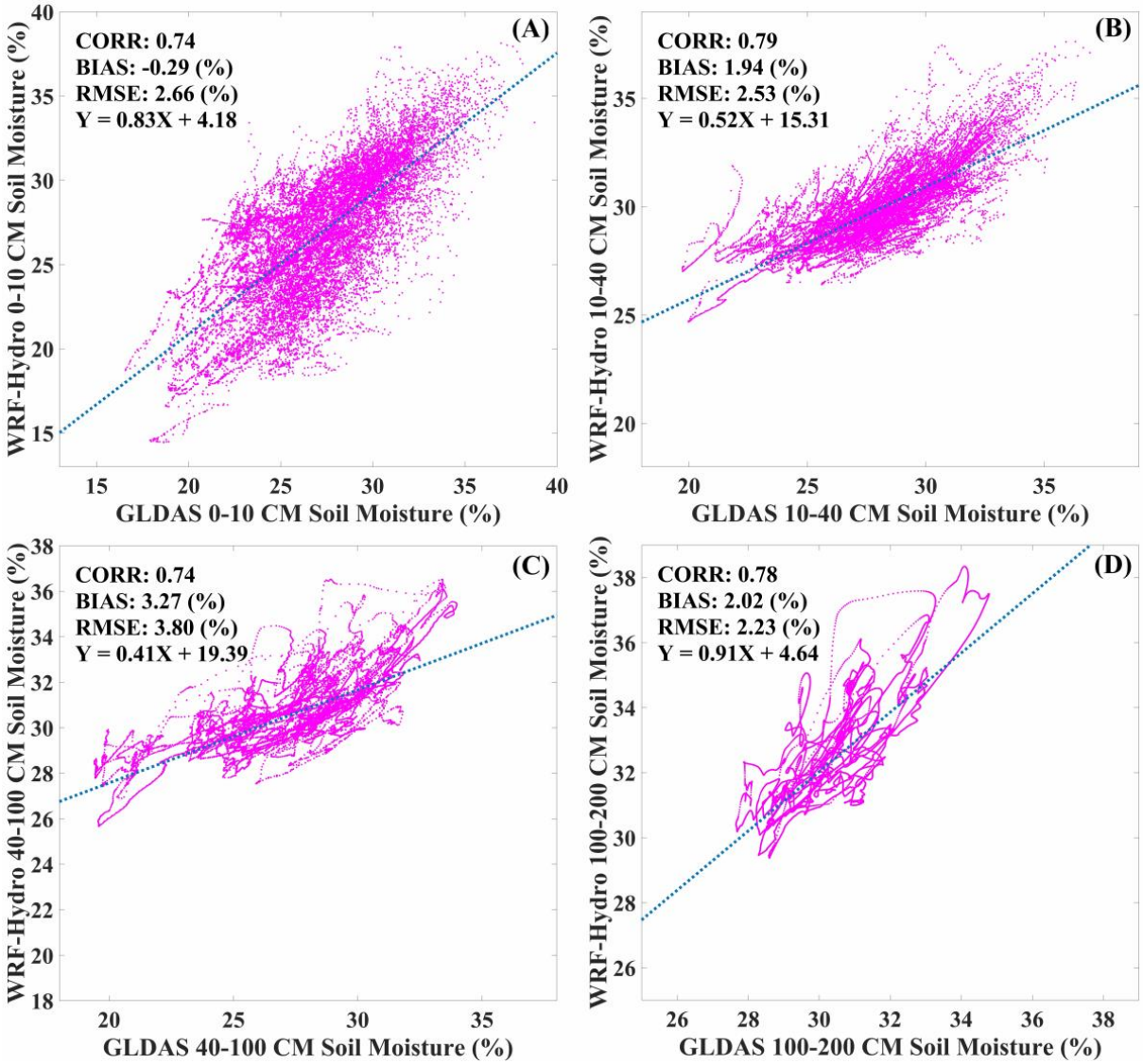

Figure 2. Scatter plots of spatially averaged soil moisture content at four depths for WRF-Hydro and GLDAS products in the Huai River Basin (2012–2018). Subplot (**A**): 0–10 cm; Subplot (**B**): 10–40 cm; Subplot (**C**): 40–100 cm; and Subplot (**D**): 100–200 cm.

Figure 3 presents a comparison of the spatial distribution of the soil moisture content at the 0–10 cm depth between two datasets, WRF-Hydro and GLDAS, across the HRB during the 7-year period from 2012 to 2018. The results show significant spatial consistency between the WRF-Hydro model and GLDAS data, demonstrating the model's ability to capture the soil moisture dynamics within the basin. For example, the GLDAS data reveal lower soil moisture content in the central-western plains of the HRB compared to the surrounding areas—a pattern that is also well-represented in the WRF-Hydro simulations. This agreement highlights the model's capacity to accurately depict spatial variability in soil moisture. However, discrepancies are evident in the eastern coastal regions of the HRB, where the WRF-Hydro model shows lower alignment with the GLDAS data. The occurrence of this phenomenon may be attributed to significant differences between CMFD precipitation data and GLDAS precipitation data in this region, resulting in soil moisture simulation outcomes being lower than those of GLDAS. Overall, although the simulation results for this region are generally underestimated, the discrepancy is not particularly large. Furthermore, Figure 3 reveals that WRF-Hydro's soil moisture simulation for January 2018 is significantly lower than in other years, suggesting that the severity of the drought this year may have been more intense. A similar phenomenon was also observed in the GLDAS results.

Figure 4 presents a time series comparison of 0–10 cm soil moisture, as simulated by the WRF-Hydro model and observed at six stations (Bozhou, Dafeng, Runan, Shangcai, Jieshou, and Suiping) within the HRB over the period from January to December 2014. The time series plots for each station are displayed side by side, enabling a direct visual comparison of the model's outputs against observational data. To evaluate the model's performance quantitatively, we calculated three metrics: the Pearson correlation coefficient (CORR), bias (BIAS), and root mean square error (RMSE) across the six stations. The results show a strong agreement between the simulated and observed soil moisture, particularly in terms of temporal variation at the 0–10 cm depth. The CORR values range from 0.72 at Runan to 0.81 at Jieshou, indicating a strong positive linear relationship between the WRF-Hydro simulations and the observational data. The BIAS values range from −5.18% at Jieshou to −0.54% at Runan, reflecting a slight tendency for the model to underestimate soil moisture. However, the magnitude of this underestimation is relatively small. Similarly, the RMSE values range from 3.12% at Runan to 5.94% at Jieshou, showcasing the model's ability to capture soil moisture dynamics with reasonable accuracy. Based on this comprehensive comparison, it can be concluded that the WRF-Hydro model performs well in simulating the 0–10 cm soil moisture at these six stations within the HRB. The model's high consistency with observational data, without significant over- or underestimations, underscores its reliability. This strong performance supports the model's suitability for subsequent drought analysis and hydrological research in the region.

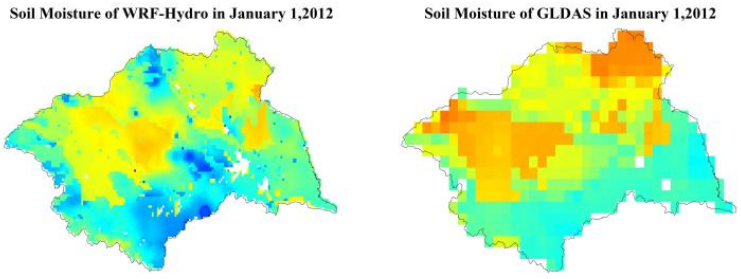

Figure 3. *Cont.*

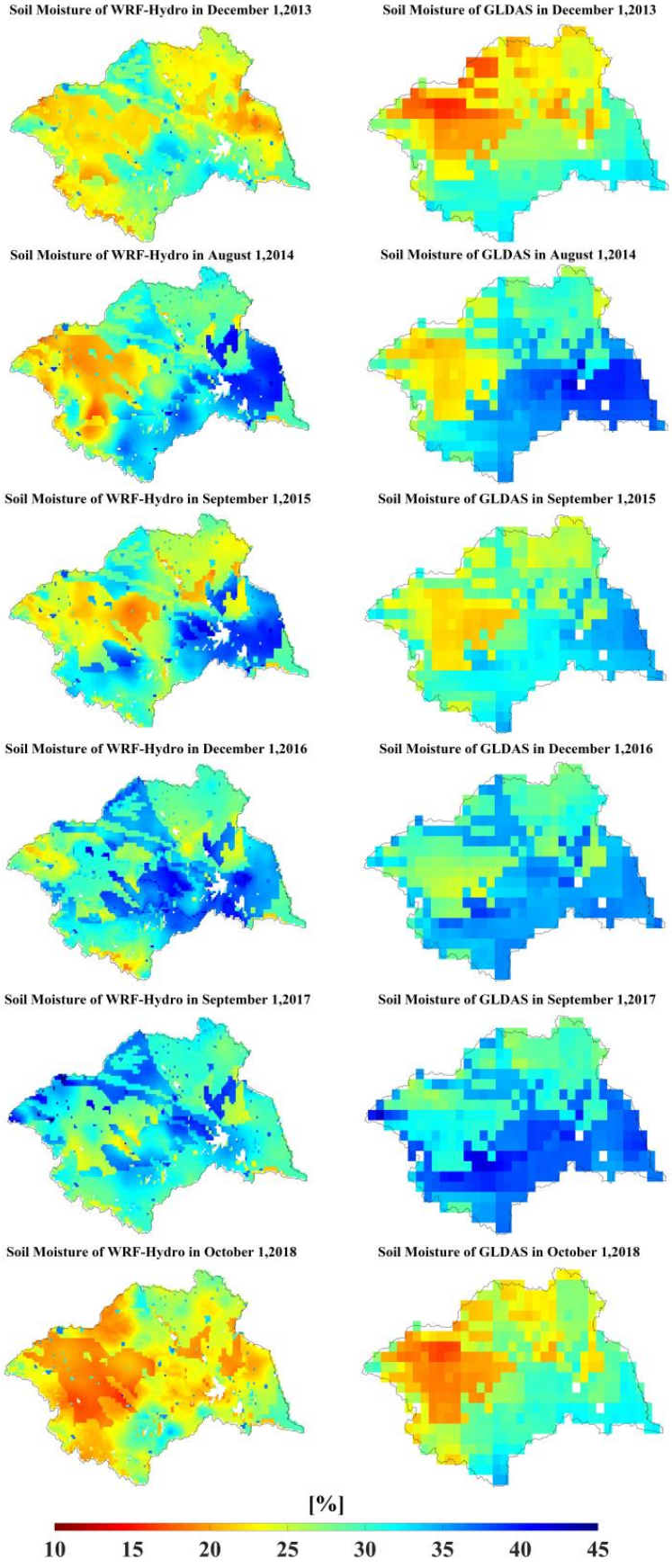

Figure 3. Comparison of spatial distribution grid maps of soil moisture content for two products (WRF-Hydro 0–10 cm and GLDAS 0–10 cm) in the Huai River Basin from 2012 to 2018.

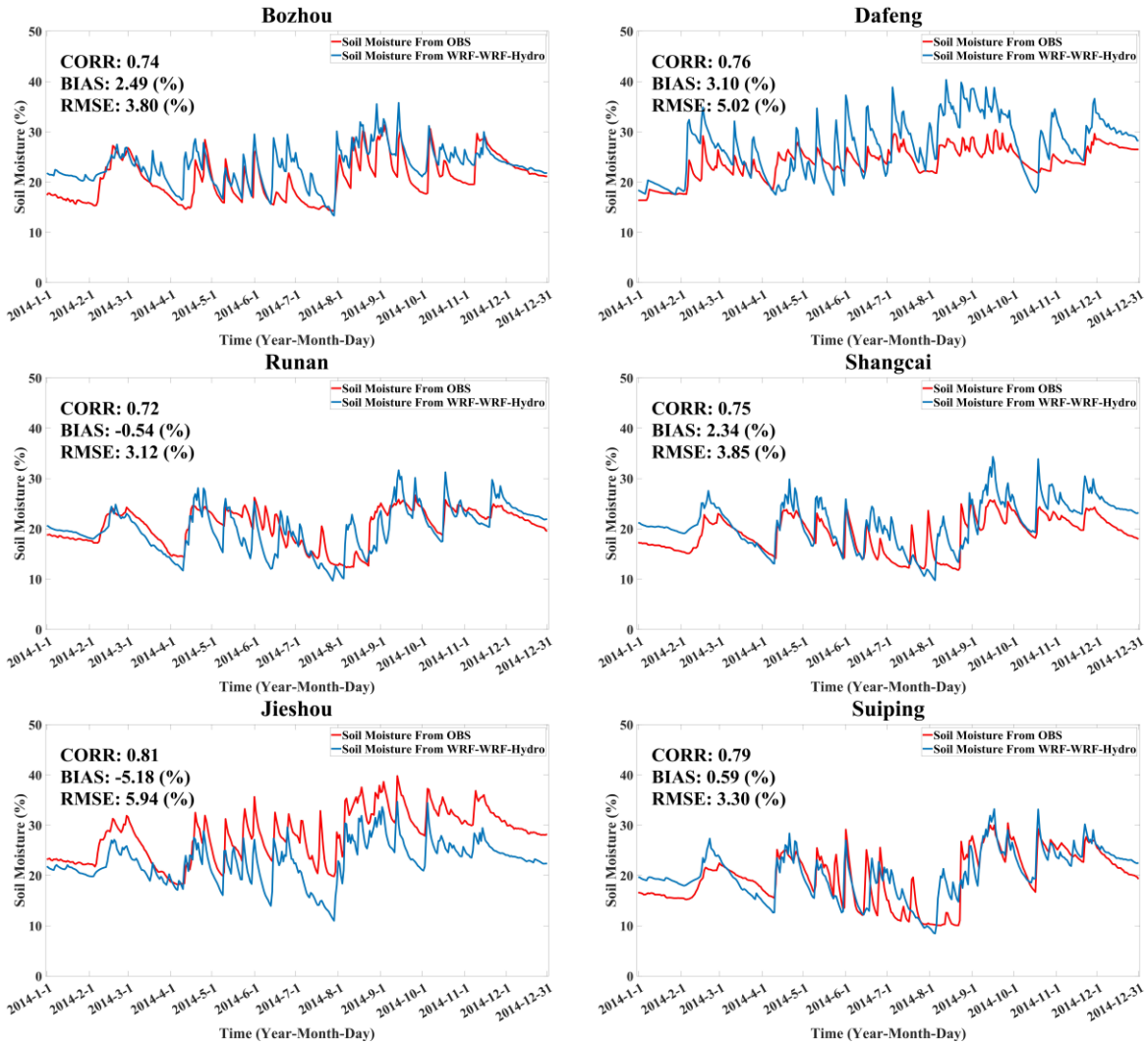

Figure 4. Time series comparison of observed and WRF-Hydro-simulated 0–10 cm soil moisture at six stations in the Huai River Basin for the year 2014.

3.2. Drought Prediction Capability of WRF-Hydro

In this section, we evaluate the drought prediction capability of the WRF-Hydro model by comparing the simulated standardized soil moisture index (SSMI) with the SSMI derived from GLDAS data, as shown in Figures 5 and 6. A similar approach was employed by Lee et al. (2022) [36], who assessed the ability of the WRF-Hydro model to monitor drought in South Korea. In their study, SSMI was calculated using both WRF-Hydro and GLDAS data to analyze agricultural drought intensity and frequency. Their findings confirmed that WRF-Hydro effectively captured drought characteristics, including frequency and intensity, thus demonstrating its reliability for drought assessments. Following this methodology, our analysis focuses on the WRF-Hydro model's performance in representing agricultural drought conditions in the HRB. This comparison provides insights into the model's accuracy and its potential for monitoring and predicting agricultural drought events in the region.

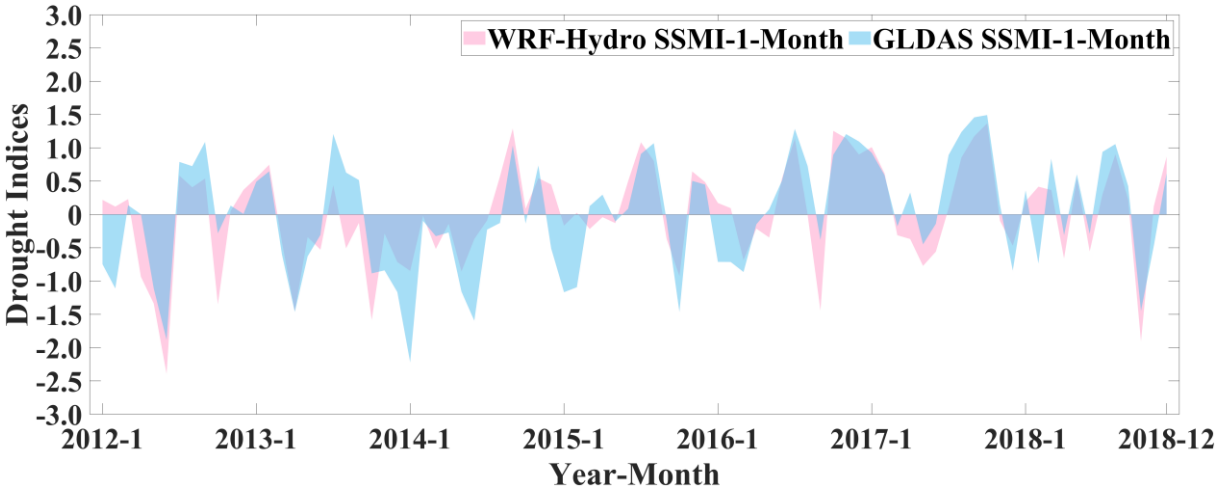

Figure 5. Time series of 1-month scale SSMI from WRF-Hydro simulation results and GLDAS data in the Huai River Basin from 2012 to 2018.

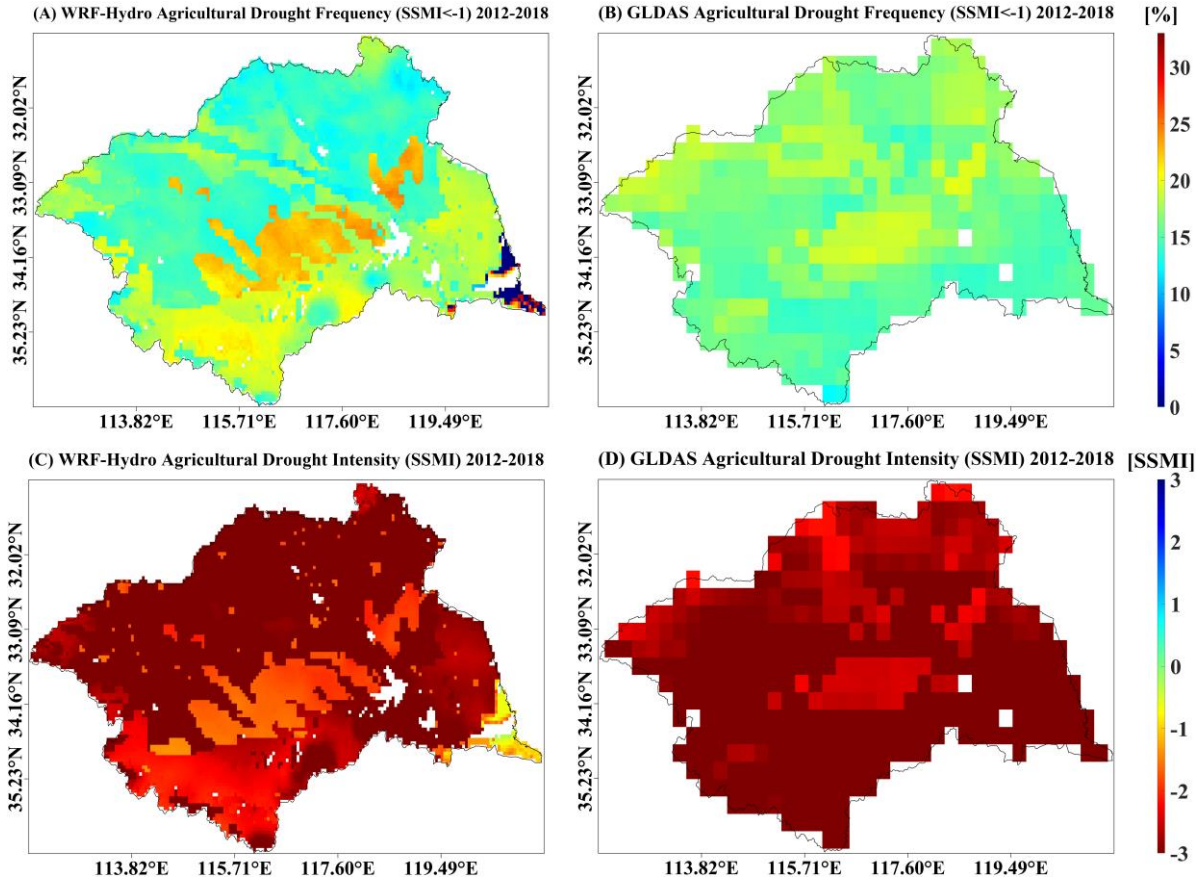

Figure 6. The spatial distribution of frequency and intensity of moderate agricultural drought events (SSMI < −1) from WRF-Hydro simulation results and GLDAS data in the Huai River Basin from 2012 to 2018.

Figure 5 compares the long-term agricultural drought index for the HRB from 2012 to 2018, as calculated by the WRF-Hydro model and GLDAS data. Over the course of nearly 84 months, the WRF-Hydro model effectively captures the overall trend of agricultural drought conditions, with the SSMI simulations aligning well with the GLDAS data. However, some fluctuations are evident in the SSMI values derived from the WRF-Hydro model. These fluctuations, along with differences between the model's simulated SSMI and the

GLDAS-derived values, can be partially attributed to the disparity in spatial resolution: GLDAS data have a resolution of 0.25°, while the WRF-Hydro model operates at 0.05°. This resolution difference could contribute to the observed variations in the standardized soil moisture index. Despite these discrepancies, the WRF-Hydro model successfully identifies almost all drought events in the basin. However, based on the figure, it is not possible to definitively determine whether the WRF-Hydro model tends to underestimate or overestimate agricultural drought conditions in the HRB compared to the GLDAS data.

Figure 6 further illustrates the spatial distribution of moderate agricultural drought events (SSMI < −1) in terms of both frequency and intensity. Panels A and B show the percentage of time that agricultural droughts (SSMI < −1) occurred during the 8-year period from 2012 to 2018, as calculated from the WRF-Hydro simulation results and the GLDAS dataset, respectively. These panels represent the agricultural drought frequency. Panels C and D display the minimum SSMI values, which represent the agricultural drought intensity over the same period, based on the WRF-Hydro model and GLDAS data, respectively. According to Panel A, the central-southern and central-eastern regions of the HRB experienced the highest frequency of agricultural droughts, with an occurrence rate of about 25%. The WRF-Hydro model's results in these areas closely match those from the GLDAS dataset. Panel C indicates that the WRF-Hydro model predicted lower drought intensity in the central-southern and central-eastern parts of the basin, while other areas generally experienced more severe droughts during the 2012–2018 period, which is a pattern consistent with the GLDAS-derived results shown in Panel D. However, the WRF-Hydro model's simulations, as shown in Panels A and C, suggest a lower frequency and weaker intensity of droughts in the eastern coastal areas of the HRB, which contrasts with the GLDAS dataset. This discrepancy may be attributed to differences in how the two models handle coastal processes, such as the influence of sea breezes or the local water table, which can affect soil moisture and, consequently, the SSMI. Despite the spatial resolution difference—0.05° for WRF-Hydro and 0.25° for GLDAS—this disparity did not significantly affect the overall spatial trends observed between the two SSMI datasets. The consistency in capturing drought events confirms that the WRF-Hydro model is proficient in predicting agricultural droughts in the HRB, validating its capability for accurate drought prediction.

3.3. Drought Characteristics in the Huai River Basin

Figure 7 presents the time series distribution of three drought indices for the HRB, calculated using precipitation data from the CMFD and soil moisture and streamflow data simulated by the WRF-Hydro model. Figure 8 provides a spatial analysis illustrating the frequency and intensity of drought events across the basin during the study period.

Figure 7 reveals that meteorological droughts occurred more frequently and with greater intensity than agricultural and hydrological droughts during the study period. For example, at a one-month timescale, mild meteorological droughts ($-1 < SPI < -0.5$) were observed 14 times, compared to 13 occurrences of mild agricultural droughts ($-1 < SSMI < -0.5$) and 14 occurrences of mild hydrological droughts ($-1 < SSFI < -0.5$). Moderate meteorological droughts ($-1.5 < SPI < -1$) occurred three times, while moderate agricultural droughts ($-1.5 < SSMI < -1$) occurred four times, and no moderate hydrological droughts ($-1.5 < SSFI < -1$) were observed. Severe meteorological droughts ($-2 < SPI < -1.5$) were recorded four times, severe agricultural droughts ($-2 < SSMI < -1.5$) occurred twice, and severe hydrological droughts ($-2 < SSFI < -1.5$) were not observed. This pattern highlights that meteorological droughts in the HRB are more frequent and intense compared to agricultural and hydrological droughts. On average, mild meteorological droughts occurred 2.0 months per year, moderate meteorological droughts occurred 0.4 months per year, and severe meteorological droughts occurred

0.6 months per year. In contrast, mild agricultural droughts occurred 1.9 months per year, moderate agricultural droughts 0.6 months per year, and severe agricultural droughts 0.3 months per year. Mild hydrological droughts occurred for 2.0 months per year, but no moderate or severe hydrological droughts were observed during the study period. These results suggest that while meteorological droughts are more prevalent, agricultural droughts occasionally display similar frequencies. The higher frequency and intensity of meteorological droughts can be attributed to the propagation of drought conditions from meteorological to agricultural and, subsequently, to hydrological systems. However, during this propagation process, the intensity and frequency of drought events are diminished. Specifically, when comparing agricultural and hydrological droughts, it is evident that hydrological droughts occur less frequently and with lower intensity than agricultural droughts. This attenuation is due to the buffering capacity of land surface and water systems, which mitigate the impacts of reduced precipitation, thereby reducing the severity and frequency of downstream drought effects.



Figure 7. Time series of 1-month scale SPI, SSMI, and SSFI in the Huai River Basin from 2012 to 2018.

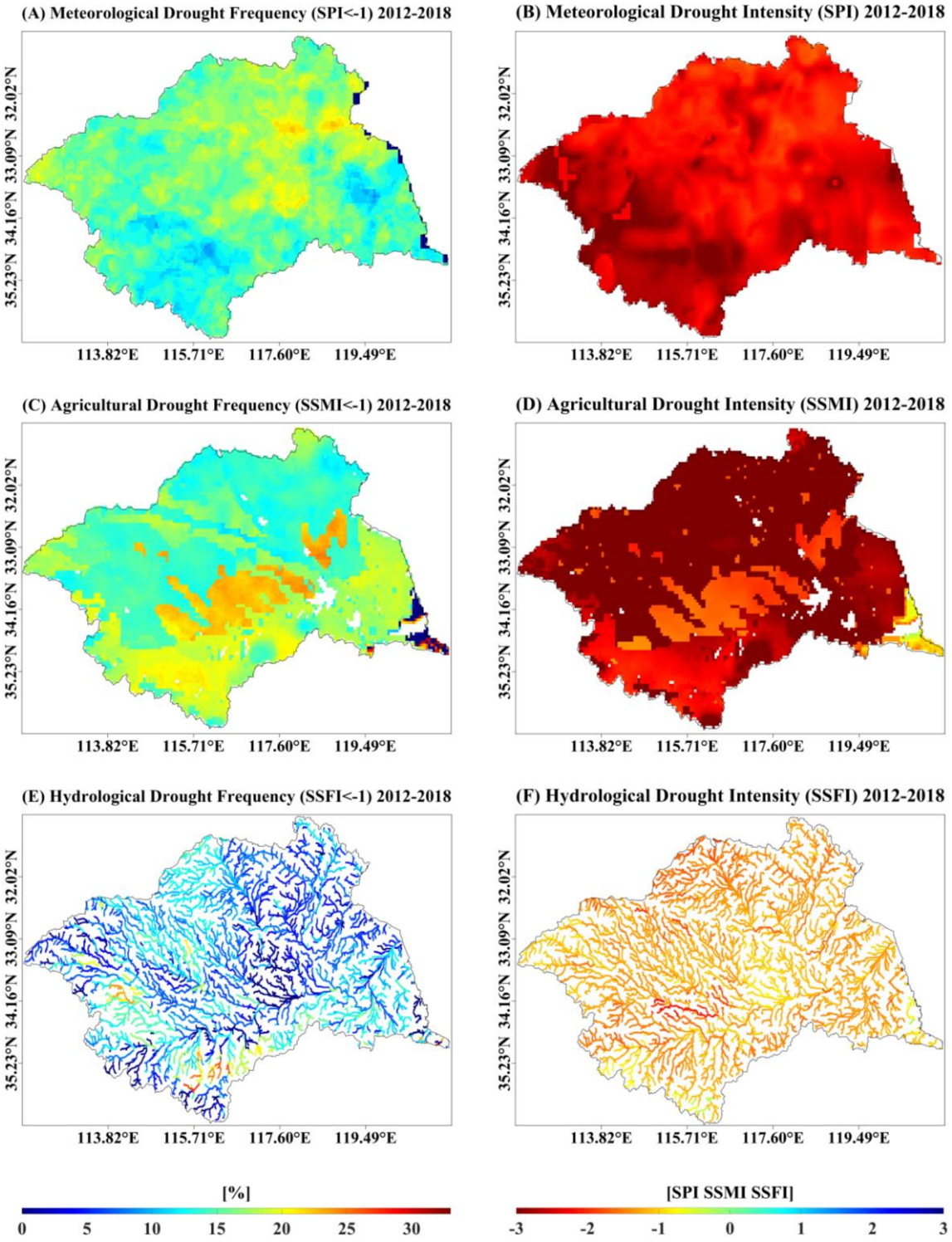

Figure 8. Frequency and intensity of meteorological, agricultural, and hydrological drought events (SPI, SSMI, SSFI < −1) in the Huai River Basin from 2012 to 2018 (minimum values of SPI, SSMI, and SSFI).

Figure 8 presents the frequency and intensity of three types of droughts—meteorological (Subplots A and B), agricultural (Subplots C and D), and hydrological (Subplots E and F)—based on WRF-Hydro model simulations for the HRB from 2012 to 2018. Subplot A shows that the probability of meteorological droughts across the HRB is generally low. Only a small area in the northeastern part of the basin exhibits a higher frequency of meteorological droughts, reaching up to 23%. In most other regions, the frequency of

such droughts remains below 20%. Subplot C indicates that the central-southern and central-eastern parts of the basin are more vulnerable to agricultural droughts, with the highest frequency reaching approximately 25%. In contrast, Subplot E reveals that the overall occurrence of hydrological droughts in the HRB is relatively low, with only a few localized areas in the southern and western parts of the basin experiencing high-frequency hydrological drought events during the study period. In most river systems, the frequency of hydrological droughts is notably lower. When comparing the intensity of droughts across subplots B, D, and F, it is clear that most areas of the HRB have experienced severe or extreme meteorological droughts. Subplot B highlights the widespread occurrence of such intense meteorological droughts. Meanwhile, Subplot D demonstrates that while many parts of the basin experienced severe or extreme agricultural droughts during 2012–2018, there are still regions where such intense agricultural droughts did not occur. Subplot F shows that the intensity of hydrological droughts is generally lower than that of agricultural droughts. Most rivers experienced only moderate hydrological droughts, with extreme hydrological droughts confined to a few areas. These findings underscore that the intensity of meteorological droughts in the HRB is higher than that of agricultural and hydrological droughts. Furthermore, the intensity of hydrological droughts is significantly lower than that of agricultural droughts. This attenuation in drought intensity as it propagates from meteorological to agricultural and then to hydrological systems aligns with the observations in Figure 7. The attenuation effect can be attributed to several factors. The soil moisture retention capacity of specific land types and the buffering effect of riverbeds help mitigate the impact of meteorological droughts on agricultural and hydrological conditions. Additionally, the presence of groundwater systems further buffers against short-term precipitation deficits, reducing the severity and frequency of downstream drought impacts.

3.4. Correlation and Propagation of Different Droughts

In this section, we analyze the propagation characteristics of meteorological drought events compared to agricultural and hydrological drought events in the HRB over an 84-month time series using drought indices. Figure 9 illustrates a notable time lag between meteorological and agricultural drought events, with agricultural droughts typically lagging by approximately one month. A comparison of the SSMI (Soil Moisture Stress Index) and SPI (standardized precipitation index) time series revealed the following: mild agricultural droughts ($-1 < \text{SSMI} < -0.5$) occurred 13 times, while mild meteorological droughts ($-1 < \text{SPI} < -0.5$) were recorded 14 times. Moderate agricultural droughts ($-1.5 < \text{SSMI} < -1$) were observed four times, compared to three occurrences of moderate meteorological droughts ($-1.5 < \text{SPI} < -1$). Severe agricultural droughts ($-2 < \text{SSMI} < -1.5$) occurred only twice, while severe meteorological droughts ($-2 < \text{SPI} < -1.5$) were identified four times. These findings suggest that although the HRB experienced moderate or severe meteorological droughts, these events often propagated as mild or moderate agricultural droughts. This indicates a reduction in drought intensity during the transition from meteorological to agricultural conditions. On average, the basin experiences mild meteorological droughts ($-1 < \text{SPI} < -0.5$) for 2.0 months per year, while mild agricultural droughts ($-1 < \text{SSMI} < -0.5$) occur for 1.9 months annually. Moderate meteorological droughts ($-1.5 < \text{SPI} < -1$) are encountered for 0.4 months per year, while moderate agricultural droughts ($-1.5 < \text{SSMI} < -1$) last for 0.6 months annually. Severe meteorological droughts ($-2 < \text{SPI} < -1.5$) occur for 0.6 months each year compared to 0.3 months for severe agricultural droughts ($-2 < \text{SSMI} < -1.5$). This indicates that severe agricultural droughts occur less frequently than severe meteorological droughts. Interestingly, the frequency of moderate agricultural droughts may exceed that of moderate meteorological droughts. This can be attributed to the attenuation effect, where severe

meteorological droughts diminish to moderate levels during propagation, leading to a higher frequency of moderate agricultural droughts in the basin. Figure 10 compares the Standardized Streamflow Index (SSFI), derived from WRF-Hydro model simulations of streamflow with the SPI calculated from CMFD precipitation data to evaluate the intensity, lag, and frequency of hydrological droughts relative to meteorological droughts. The results reveal that hydrological droughts in the HRB generally exhibit a lower intensity than meteorological droughts. For instance, mild hydrological droughts ($-1 < \text{SSFI} < -0.5$) occurred 14 times, matching the 14 occurrences of mild meteorological droughts ($-1 < \text{SPI} < -0.5$). However, no moderate hydrological droughts ($-1.5 < \text{SSFI} < -1$) were recorded, contrasting with three occurrences of moderate meteorological droughts ($-1.5 < \text{SPI} < -1$). This discrepancy highlights the significant attenuation of drought intensity as meteorological droughts propagate into hydrological systems.

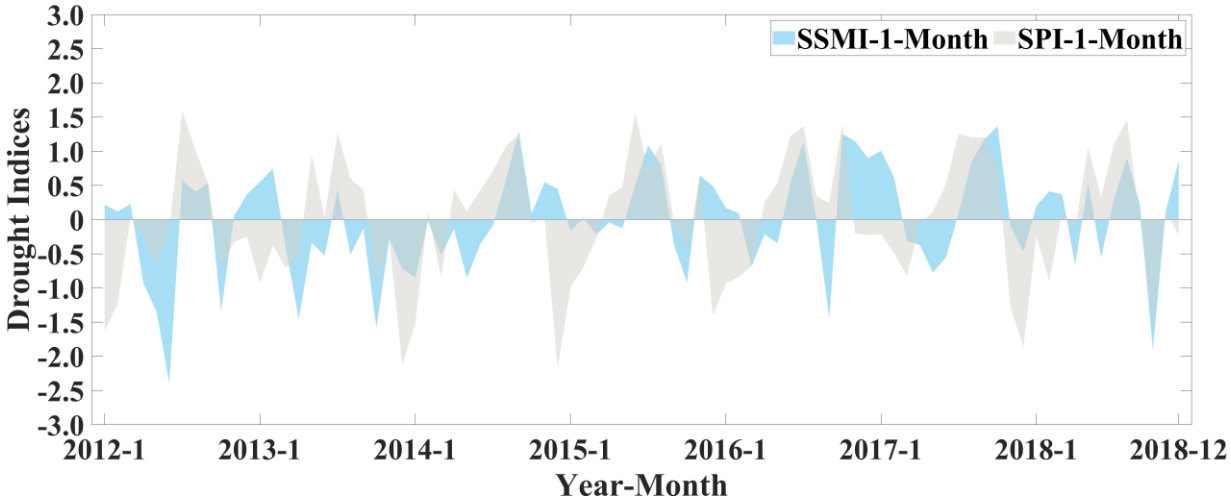

Figure 9. The time series of SSMI calculated from WRF-Hydro-simulated soil moisture and SPI calculated from CMFD precipitation data from 2012 to 2018.

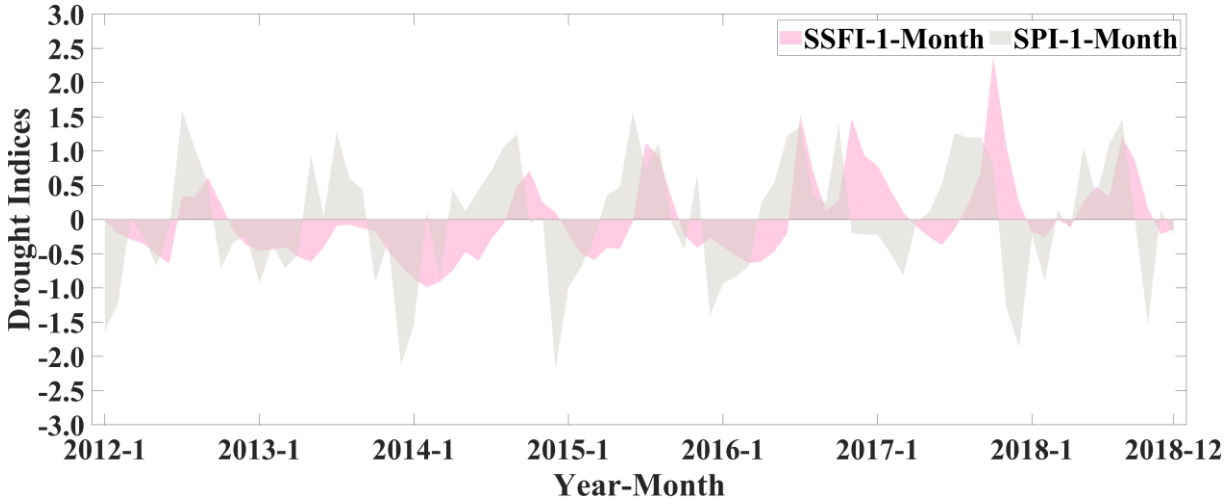

Figure 10. The time series of SSFI calculated from WRF-Hydro-simulated streamflow data and SPI calculated from CMFD precipitation data from 2012 to 2018.

Similarly to our findings, studies in other regions have also documented lags and changes in intensity during the propagation of meteorological drought into hydrological and agricultural droughts. For instance, Lee et al. (2022) [36] examined the temporal lag and intensity variations between meteorological drought (measured by the standardized

precipitation index, SPI) and hydrological drought (measured by the Standardized Streamflow Index, SSFI) during drought propagation in South Korea. Their study revealed that hydrological drought events typically lagged behind meteorological drought events by 18 to 32 days at the 3-month timescale and by 30 to 60 days at the 6-month timescale, depending on the region and drought index used. Furthermore, the intensity of hydrological drought tended to diminish as it propagated from meteorological drought, with this attenuation effect being more pronounced at longer timescales. This indicates that severe meteorological droughts are gradually alleviated as they transition into the hydrological system. However, this study observed no significant lag between agricultural and hydrological droughts, with the relationship between these two types of droughts varying across regions. Notable drought events, such as those in December 2013, December 2014, December 2015, and December 2017, showed that severe or moderate meteorological droughts often resulted in only mild or no hydrological droughts. This finding underscores the significant weakening of drought intensity during its transition from meteorological to hydrological phases, suggesting that surface water systems act as buffers against precipitation deficits. Monthly comparisons of SSFI and SPI from January 2012 to January 2018 further support this pattern, consistently showing that hydrological drought lags behind meteorological drought by approximately one month. This lag can be attributed to the delay in converting surface precipitation into runoff, which is a process influenced by factors such as soil moisture storage, groundwater recharge, and evapotranspiration. In the HRB, annual drought statistics reveal that mild meteorological droughts ($-1 < \text{SPI} < -0.5$) occur for an average of 2.0 months per year, moderate meteorological droughts ($-1.5 < \text{SPI} < -1$) occur for 0.4 months, and severe meteorological droughts ($-2 < \text{SPI} < -1.5$) occur for 0.6 months. In contrast, mild hydrological droughts ($-1 < \text{SSFI} < -0.5$) are observed for an average of 2.0 months per year, with no recorded occurrences of moderate or severe hydrological droughts. This pattern confirms that both the intensity and frequency of hydrological droughts are generally lower than those of meteorological droughts.

4. Conclusions

This study employed the WRF-Hydro model and multiple standardized drought indices, including the SPI, SSMI, and SSFI, to analyze drought dynamics in the HRB from 2012 to 2018. By comparing model outputs with GLDAS data and soil moisture observations from monitoring stations, the accuracy of the model's simulations was rigorously assessed. This study evaluates drought intensity and frequency while systematically exploring the interactions and time lags among meteorological, agricultural, and hydrological droughts, providing an integrated view of drought propagation in the HRB.

The results demonstrate that the WRF-Hydro model effectively captures the spatial and temporal variability of drought events, showing strong agreement with GLDAS data. For soil moisture at a depth of 0–10 cm, the model achieved a CORR of 0.74, a BIAS of -0.29, and a RMSE of 2.66%, validating its reliability in near-surface soil moisture simulations. Comparisons with soil moisture data from six monitoring stations yielded an overall CORR of 0.75, with the highest value reaching 0.81, indicating no significant underestimation or overestimation by the model. Analysis of the drought indices revealed that meteorological droughts typically precede agricultural and hydrological droughts by about one month. This study highlights that the frequency and intensity of agricultural and hydrological droughts are generally lower than those of meteorological droughts, reflecting the buffering effects of surface and subsurface systems. These attenuation effects are particularly notable during the transition from meteorological to hydrological droughts, underscoring the complex interactions between different drought types within the basin. While the WRF-Hydro model proves to be a robust tool for drought monitoring and prediction, limitations

remain. Default parameterizations and differences in spatial resolution between the WRF-Hydro model and GLDAS data contribute to some discrepancies in drought intensity and frequency estimates. Future research should focus on refining model parameters and incorporating additional observational datasets, particularly for soil moisture and streamflow, to enhance predictive accuracy.

In conclusion, this study highlights the significant potential of the WRF-Hydro model to simulate drought dynamics in the HRB. The findings provide valuable insights for improving water resource management, enhancing drought early warning systems, and mitigating future drought impacts in the region. Future studies should aim to optimize model performance through parameter calibration and assess the impacts of climate change on drought propagation in this ecological and economically critical basin.

Author Contributions: Conceptualization, Y.Y.; methodology, Y.Y. and Y.Z.; software, Y.Z.; validation, Y.H.; data curation, Z.T. and H.H.; writing—original draft preparation, Y.Z. and Y.Y.; supervision, Y.L. All authors have read and agreed to the published version of the manuscript.

Funding: This research was funded by the National Natural Science Foundation of China (grant number 42101361), the China Postdoctoral Science Foundation (2024M753092), the Key Research and Development Program of Anhui (2022m07020003), and the Jianghuai Meteorological Joint Project of Anhui Natural Science Foundation (2408055UQ006), the Scientific Research Project of Higher Education Institutions in Anhui Province (2023AH050143), National Undergraduate Innovation and Entrepreneurship Training Program (202310370056, 202310370051). And the APC was funded by 2408055UQ006.

Data Availability Statement: The China Meteorological Forcing Dataset used in this study can be downloaded online in the website: https://data.tpdc.ac.cn, accessed on 29 October 2024.

Conflicts of Interest: The authors declare no conflict of interest.

References

1. Banholzer, S.; Kossin, J.; Donner, S. The impact of climate change on natural disasters. In *Reducing Disaster: Early Warning Systems for Climate Change*; Springer: Dordrecht, The Netherlands, 2014; pp. 21–49. [CrossRef]
2. Cammalleri, C.; Naumann, G.; Mentaschi, L.; Formetta, G.; Forzieri, G.; Gosling, S.; Feyen, L. *Global Warming and Drought Impacts in the EU*; Publications Office of the European Union: Luxembourg, 2020.
3. Cook, B.I.; Mankin, J.S.; Anchukaitis, K.J. Climate change and drought: From past to future. *Curr. Clim. Chang. Rep.* **2018**, *4*, 164–179. [CrossRef]
4. Arabameri, A.; Chandra Pal, S.; Santosh, M.; Chakrabortty, R.; Roy, P.; Moayedi, H. Drought risk assessment: Integrating meteorological, hydrological, agricultural and socio-economic factors using ensemble models and geospatial techniques. *Geocarto Int.* **2022**, *37*, 6087–6115. [CrossRef]
5. Thober, S.; Kumar, R.; Sheffield, J.; Mai, J.; Schäfer, D.; Samaniego, L. Seasonal soil moisture drought prediction over Europe using the North American Multi-Model Ensemble (NMME). *J. Hydrometeorol.* **2015**, *16*, 2329–2344. [CrossRef]
6. Zhong, F.; Cheng, Q.; Wang, P. Meteorological drought, hydrological drought, and NDVI in the Heihe River basin, Northwest China: Evolution and propagation. *Adv. Meteorol.* **2020**, *2020*, 2409068. [CrossRef]
7. Van Loon, A.F. Hydrological drought explained. *WIREs Water* **2015**, *2*, 359–392. [CrossRef]
8. Hisdal, H.; Tallaksen, L.M.; Gauster, T.; Bloomfield, J.P.; Parry, S.; Prudhomme, C.; Wanders, N. Hydrological drought characteristics. In *Hydrological Drought*; Elsevier: Amsterdam, The Netherlands, 2024; pp. 157–231. [CrossRef]
9. Marusov, A.; Grabar, V.; Maximov, Y.; Sotiriadi, N.; Bulkin, A.; Zaytsev, A. Long-term drought prediction using deep neural networks based on geospatial weather data. *arXiv* **2023**, arXiv:2309.06212. [CrossRef]
10. Zhang, B.; Salem, F.K.A.; Hayes, M.J.; Tadesse, T. Quantitative assessment of drought impacts using XGBoost based on the Drought Impact Reporter. *arXiv* **2022**, arXiv:2211.02768. [CrossRef]
11. Nandgude, N.; Singh, T.P.; Nandgude, S.; Tiwari, M. Drought prediction: A comprehensive review of different drought prediction models and adopted technologies. *Sustainability* **2023**, *15*, 11684. [CrossRef]
12. Wang, W.; Ertsen, M.W.; Svoboda, M.D.; Hafeez, M. Propagation of drought: From meteorological drought to agricultural and hydrological drought. *Adv. Meteorol.* **2016**, *2016*, 6547209. [CrossRef]

13. Zhang, X.; Hao, Z.; Singh, V.P.; Zhang, Y.; Feng, S.; Xu, Y.; Hao, F. Drought propagation under global warming: Characteristics, approaches, processes, and controlling factors. *Sci. Total Environ.* **2022**, *838*, 156021. [CrossRef]
14. Bae, H.; Ji, H.; Lim, Y.J.; Ryu, Y.; Kim, M.H.; Kim, B.J. Characteristics of drought propagation in South Korea: Relationship between meteorological, agricultural, and hydrological droughts. *Nat. Hazards* **2019**, *99*, 1–16. [CrossRef]
15. Zhao, L.; Lyu, A.; Wu, J.; Hayes, M.; Tang, Z.; He, B.; Liu, M. Impact of meteorological drought on streamflow drought in Jinghe River Basin of China. *Chin. Geogr. Sci.* **2014**, *24*, 694–705. [CrossRef]
16. Gu, L.; Chen, J.; Yin, J.; Xu, C.Y.; Chen, H. Drought hazard transferability from meteorological to hydrological propagation. *J. Hydrol.* **2020**, *585*, 124761. [CrossRef]
17. Zhao, L.; Wu, J.; Fang, J. Robust response of streamflow drought to different timescales of meteorological drought in Xiangjiang River Basin of China. *Adv. Meteorol.* **2016**, *2016*, 1634787. [CrossRef]
18. Wu, J.; Chen, X.; Yao, H.; Zhang, D. Multi-timescale assessment of propagation thresholds from meteorological to hydrological drought. *Sci. Total Environ.* **2021**, *765*, 144232. [CrossRef]
19. Shukla, S.; Wood, A.W. Use of a standardized runoff index for characterizing hydrologic drought. *Geophys. Res. Lett.* **2008**, *35*, L02401. [CrossRef]
20. Crow, W.T.; Su, C.H.; Ryu, D.; Yilmaz, M.T. Optimal averaging of soil moisture predictions from ensemble land surface model simulations. *Water Resour. Res.* **2015**, *51*, 9273–9289. [CrossRef]
21. Barella-Ortiz, A.; Quintana-Seguí, P. Evaluation of drought representation and propagation in regional climate model simulations across Spain. *Hydrol. Earth Syst. Sci.* **2019**, *23*, 5111–5131. [CrossRef]
22. Yoo, J.Y.; Song, H.; Kim, T.W.; Ahn, J.H. Evaluation of short-term drought using daily standardized precipitation index and ROC analysis. *KSCE J. Civ. Environ. Eng. Res.* **2013**, *33*, 1851–1860. [CrossRef]
23. Kilicarslan, B.M.; Temimi, M. Simulating block-scale flood inundation and streamflow using the WRF-Hydro model in the New York City metropolitan area. *Natur. Haz.* **2024**, *120*, 10043–10066. [CrossRef] [PubMed]
24. Lin, P.; Rajib, M.A.; Yang, Z.L.; Somos-Valenzuela, M.; Merwade, V.; Maidment, D.R.; Chen, L. Spatiotemporal evaluation of simulated evapotranspiration and streamflow over Texas using the WRF-Hydro-RAPID modeling framework. *J. Am. Water Resour. Assoc.* **2018**, *54*, 40–54. [CrossRef]
25. Arnault, J.; Wagner, S.; Rummler, T.; Fersch, B.; Bliefernicht, J.; Andresen, S.; Kunstmann, H. Role of runoff-infiltration partitioning and resolved overland flow on land-atmosphere feedbacks: A case study with the WRF-Hydro coupled modeling system for West Africa. *J. Hydrometeorol.* **2016**, *17*, 1489–1516. [CrossRef]
26. Givati, A.; Gochis, D.; Rummler, T.; Kunstmann, H. Comparing one-way and two-way coupled hydrometeorological forecasting systems for flood forecasting in the Mediterranean region. *Hydrology* **2016**, *3*, 19. [CrossRef]
27. Yu, M.; Liu, X.; Li, Q. Responses of meteorological drought-hydrological drought propagation to watershed scales in the upper Huaihe River basin, China. *Environ. Sci. Pollut. Res.* **2020**, *27*, 17561–17570. [CrossRef] [PubMed]
28. Wang, J.; Wang, W.; Cheng, H.; Wang, H.; Zhu, Y. Propagation from meteorological to hydrological drought and its influencing factors in the Huaihe River Basin. *Water* **2021**, *13*, 1985. [CrossRef]
29. Sun, M.; Liu, A.; Zhao, L.; Wang, C.; Yang, Y. Evaluation of Multi-Source Precipitation Products in the Hinterland of the Tibetan Plateau. *Atmosphere* **2024**, *15*, 138. [CrossRef]
30. Edwards, D.C.; McKee, T.B. *Characteristics of 20th Century Drought in the United States at Multiple Time Scales*; Colorado State University: Fort Collins, CO, USA, 1997.
31. McKee, T.B.; Doesken, N.J.; Kleist, J. The relationship of drought frequency and duration to time scales. In Proceedings of the 8th Conference on Applied Climatology, Anaheim, CA, USA, 17–22 January 1993; pp. 179–183.
32. Angelidis, P.; Maris, F.; Kotsovinos, N.; Hrissanthou, V. Computation of drought index SPI with alternative distribution functions. *Water Resour. Manag.* **2012**, *26*, 2453–2473. [CrossRef]
33. Lloyd-Hughes, B.; Saunders, M.A. A drought climatology for Europe. *Int. J. Climatol.* **2002**, *22*, 1571–1592. [CrossRef]
34. Guttman, N.B. Accepting the standardized precipitation index: A calculation algorithm. *J. Am. Water Resour. Assoc.* **1999**, *35*, 311–322. [CrossRef]
35. Wang, W.; Cui, W.; Wang, X.; Chen, X. Evaluation of GLDAS-1 and GLDAS-2 forcing data and Noah model simulations over China at the monthly scale. *J. Hydrometeorol.* **2016**, *17*, 2815–2833. [CrossRef]
36. Lee, J.; Kim, Y.; Wang, D. Assessing the characteristics of recent drought events in South Korea using WRF-Hydro. *J. Hydrol.* **2022**, *607*, 127459. [CrossRef]

Disclaimer/Publisher's Note: The statements, opinions and data contained in all publications are solely those of the individual author(s) and contributor(s) and not of MDPI and/or the editor(s). MDPI and/or the editor(s) disclaim responsibility for any injury to people or property resulting from any ideas, methods, instructions or products referred to in the content.